

# Analysing Closed-Fringe Images using 2D Fan Wavelets

S. Dehaeck, Y. Tsoumpas & P. Colinet<sup>1</sup>

<sup>1</sup>Université Libre de Bruxelles, TIPs (Transfers, interfaces and Processes), CP 165/67,  
Av. F.D. Roosevelt 50, 1050 Brussels, Belgium\*

compiled: February 20, 2015

In this paper, it will be shown how the use of two 2D Fan wavelets to analyse closed-fringe images can lead to a relatively fast and exceptionally noise-resistant algorithm capable of extracting not only local phase but also local frequency information. Our algorithm is up to 10 times faster than the current state-of-the-art in Wavelet processing techniques and even up to 30 times faster than 'Windowed Fourier' Transform programs which achieve similar noise-resiliency figures. This improvement is mainly achieved by the use of Fan wavelets instead of Morlet wavelets, but a more efficient scale-space discretisation strategy is also described and three different alternatives are suggested capable of solving the phase sign ambiguity problem in a quick and efficient manner. Finally, the application of the algorithm to real and numerically generated images shows that a precision of 1/30th of a fringe is achievable for noise levels going up to 1/5th of the input contrast.

*OCIS codes:* (120.2650) Fringe analysis; (100.5070) Phase retrieval; (100.7410) Wavelets; (120.5050) Phase measurement; (120.6160) Speckle interferometry; (120.3940) Metrology

<http://dx.doi.org/10.1364/XX.99.099999>

## 1. Introduction

Interferometry is a classical technique capable of measuring minute optical path length differences accurately. These differences can be generated by refractive index changes in the traversed medium due to temperature variations (e.g. [1]) or compositional changes in the liquid phase (e.g. [2]) or gas phase (e.g. [3]). However, these variations can generally be neglected when thickness variations are present in the observed object. In this case, equal-thickness fringes appear (similar to Newton's rings) where each closed fringe represents a well-defined thickness. For instance, here, such images are coming from evaporating sessile droplets on a flat surface with maximal slopes below 20°, imaged in a standard Mach-Zehnder interferometer. The most important parameters that we want to characterise correctly are the 3D droplet shape, its volume and importantly also its contact angle, i.e. the finite angle the liquid interface makes with the surface at the location where the liquid reaches a zero thickness.

A straightforward approach to analysing interferometric images is by fringe skeletonization in which the centre of the white and black fringes are localised and are attributed a given height (e.g. [4]). However, with

the advent of CCD-cameras and more powerful computers, one would rather aim to obtain height information in each pixel. Thus, papers have appeared in literature (e.g. [5]) which perform a sort of Look-Up Table approach (LUT) where each digital gray scale value is converted to a certain phase after a suitable assignment of 'black' and 'white' intensity values to 0 and  $\pi$  phase differences (which may vary over the image). In the so-called Reflective Interference Contrast Microscopy method used for instance by Wiegand et al [6] and by De Ruiter et al [7] such intensity look-up tables are also used. Common to these LUT-based methods is that they work on the individual pixel level and therefore the phase error is directly proportional to the intensity noise level of the camera.

In contrast, in the present work some sort of 'spatial smoothing' will be applied in order to obtain more precise results in the presence of noise. This 'smoothing' is done through the analysis of the spatial variation of the intensity in the image. This can be done with many different analysis techniques such as the Fourier-transform method (e.g. [8]), the spiral phase transform (or 2D-Hilbert transform) (e.g. [9]), the windowed Fourier Transform [10] and the Wavelet Ridge (WR) technique (e.g. [11, 12]). While each of these approaches has its merits, we have chosen the WR technique here due to its good noise robustness, its capability to handle large bandwidth signals and last but not least, its contain-

---

\* sam.dehaeck@gmail.com, pcolinet@ulb.ac.be

ment of local defects [13]. Especially this last property is important in the current context as at the contact line the signal is discontinuous and with the WR-technique its disturbing effect on the measurements is confined to a small region surrounding it. In this respect, Ma et al [11, 12] have already analysed closed-fringe systems with WR techniques. However they used the Morlet wavelet which is directionally sensitive. In this manuscript, we will primarily show how the use of two 2D Fan wavelets with different orientation can speed up the analysis by up to 10 times.

Next to the phase extraction, a second issue that needs to be overcome is the sign ambiguity of the obtained phase. This sign ambiguity is caused by the fact that it is difficult to know whether the phase is locally increasing or decreasing. A classic way of solving this problem is by introducing a carrier frequency [14]. However, this reduces the maximum contact angles that we can measure and therefore is not wanted here. A second typical approach is to use phase-stepping [15] where multiple images with a uniform phase shift are used to resolve this problem. However, due to the highly dynamic nature of the evaporating droplets under study, phase-stepping is not directly tested here (but a hybrid technique is).

Another way of tackling this sign ambiguity is by solving the equivalent problem of determining the direction of the fringes (in the range 0-360°) from the obtained orientation of the fringes (angles in the range 0-180°). This is performed in two steps. First, the orientation of the fringes needs to be determined and then this is 'transformed' to a continuous direction map. For the determination of the orientation, two different approaches can be found in literature. One is working on the raw intensity data using small neighbourhood operators. Some example algorithms are the gradient method [16], the spin filter [17], the energy operator method [18], the accumulated differences method [19] and principal component analysis techniques [10]. These algorithms are all fast but rather noise-sensitive. As such, prefiltering is often (but not always) necessary, which leads to its own set of difficulties. The second approach is to use a sort of directional frequency analysis approach which is more insensitive to noise. Examples here are Ma et al [11] who used directional wavelets and Wang et al [20] who used Windowed Fourier Techniques. While these techniques show a good noise resiliency, the use of a directional frequency analysis technique is computationally very demanding. In the present manuscript, a direction insensitive frequency analysis approach is used for the phase determination, while the orientation estimation uses a fast neighbourhood operator (accumulated differences method) which

is applied to the smooth absolute phase map instead of on the noisy intensity data leading to a combination of both advantages.

The second step in solving the sign ambiguity problem is to transform the obtained orientation map into a direction map. Again, many approaches have been proposed in literature. In essence, this is similar to the phase unwrapping problem which is very familiar to the interferometric community and discussed at length in e.g. Ghiglia et al [21]. As such, some sort of cost-optimization [22, 23], multiscale [24] and quality-map guided algorithm [23, 25] has already been proposed. In the present manuscript, we have modified our unwrapping algorithm of choice (from Herraez et al [26]) to perform this task. The advantage (and novelty) of this algorithm is that it does not follow a continuous path. This avoids getting "trapped" in a bad region and is fast as the path is not build iteratively but requires only a single sorting operation. The tricky parts of the image which need to be avoided or kept as last are the stagnation points. In these points, no abrupt change in direction is detected and hence the 'sign unwrapping' fails. As these troubled points are generally co-located with local minima in the fringe frequency, the quality map used for the determination of the sign-unwrapping path tends to go from the high to the low frequency zones (e.g. [27]). However, the inverse is not necessarily true; a high frequency zone is not necessarily more reliable than a low frequency one as several real-life artifacts in interferometric images also have a high-frequency content (e.g. window scratches, dust particles). Therefore, in classical phase unwrapping, the modulation or local contrast is more often used for the quality map [28, 29]. We will show here for the first time that this is also a good choice here as the stagnation points also correspond to lower local amplitudes, thus underlining once more that the two problems (phase and sign unwrapping) can be solved by exactly the same algorithms. In the present case, we found that an even better reliability could be obtained if a second level of priority is build into the quality map which tries to avoid passing through direction-discontinuous points (similar to the original quality map [26]). Such a multi-level quality map is in some sense similar to Zhang et al [30].

While the above combination of fringe orientation estimation and transformation to direction is the usual way of analysing closed fringes, we will also suggest two alternative solutions to the sign ambiguity problem. First, for very simple images like normal droplets where only a single stagnation point is present and the image is perfectly convex, a much simpler solution is proposed which resolves the problem in a fraction of a second. Then, for very complex images where for instance a

closed stagnation line is present (for instance a volcano crater profile with a central depression and a rim), a single image is not capable of giving all the required information. For such a case, a hybrid technique using some elements of phase stepping is the easiest solution. This approach was already suggested by Kreis [8] and Ma et al [12]. In the present manuscript, we will show how to implement the method of Kreis [31] here and only highlight that this even works for highly dynamic objects where the absolute phase difference is varying across the image without this impacting the accuracy of the method, something which is absent in the technique proposed in [12].

Next to the extraction of the phase from which the droplet volume can be calculated, the contact angle is also a measurement of great interest. It will be shown here how this quantity can be derived directly from the local scale estimation obtained from the WR-technique (in the same spirit as already done for strain analysis in [32]). This avoids a lengthy post-processing step in which differentiation in variable directions would need to be performed. Because of this objective, the contact angle precision becomes directly linked to our choice of scales in the WR-technique. However, for the scale discretisation procedure, a surprising small amount of publications are available. Li et al [33] just stated a practical discretization procedure which is employed internally by Matlab and Ma et al [34] analysed the minimum amount of scales one can use to obtain a reliable phase estimate. However, as we are also interested in a precise scale estimation, a new discretization strategy will be analytically derived so as to yield a constant precision throughout the entire frequency space. In our opinion, this is also an important contribution of the present manuscript which serves to optimise the required resources so as to obtain a target precision.

In short, in the present manuscript improvements are proposed to several of the building blocks needed to analyse complex closed-fringe images. Mainly, the use of Fan wavelets instead of Morlet wavelets and the use of the accumulated differences method on the smooth absolute phase image to obtain the fringe orientation is shown to result in a dramatic speed increase in the full algorithm. With the current approach, the phase can be extracted from a 1024x1024 image in 1.9s on a four year old laptop (Intel I5-2520M, 1333Mhz RAM using Python 2.7 with the Numpy, Scipy and FFTW3 libraries). When a reasonable accuracy in local angle is required (and thus more scales), a full analysis requires +9.3s. Although no direct comparisons are given, another recent paper using WR-techniques by Ma et al [11] should in principle be approximately 10 times slower as 20 directional Morlet wavelets were used in

their case, whereas only two Fan wavelets are required here.

Another technique which is capable of giving similar noise-robust phase and frequency measurements is the Windowed Fourier transform method. In a recent publication, an optimised parallelised code was implemented on a (more) powerful computer [35] but still required 5 minutes to analyse a single image! Clearly, our algorithm is a much more viable alternative.

On a final note, we would like to stress that the analysis is fully automatic and no parameter-tuning is necessary. Even the segmentation of the droplet from the background can be done automatically.

Regarding to the structure of the current paper, we start with a general overview of the algorithm highlighting each of the separate steps. This is followed by a detailed description of each of these steps. Then, the accuracy and precision of the proposed algorithms when applied to theoretical images with varying noise levels is analysed. Finally, the algorithms are applied to real interferometric images of droplets and the performance is analysed.

## 2. Methodology

### 2.A. Overview of the algorithm

In the present manuscript, we focus on the fully automatic analysis of images such as the one shown in Fig 1(a). The different steps of our algorithm are the following. First, a 2D Wavelet Ridge (WR) algorithm is performed on the image. As the 2D Wavelet Transform is in general direction sensitive and this information is not required here, we use the complex Fan mother wavelet (as introduced by Antoine and Murenzi [36], Kirby [37] and Gdeisat et al [13]). This is in essence a combination of several complex Morlet Wavelets with different directions distanced in such a way so as to have the most uniform magnitude response possible for a range of directions. Nevertheless, it is not possible to obtain full 180° direction insensitivity. Therefore, a combination of two 2D Fan wavelets is used. One for the predominantly horizontal directions and one for the vertical ones. More details will be given in section 2.B. The information that we will retain from this step is the locally best-fitting scale, the locally best-fitting phase (including sign-ambiguity) and the amplitude for the two directions (see section 2.B.2). This results in the images shown in Fig 1(b) to (e) (local scale images are not shown due to space constraints, but they are very similar to the amplitude images). Important to notice in these images is that they seem to be divided in two parts. Focussing on Fig 1(d), which is the local amplitude after performing the Wavelet Ridge technique with the 'horizontal' Fan (i.e. sensitive to horizontal phase gradients), it is clear that the separating dark zone corresponds to

that location where the phase gradient becomes vertical. In Fig 1(b), which shows the corresponding local phase, it is clear that only coherent results are obtained in those regions where a high local amplitude is found.

We should point out here that the use of two 2D Fan wavelets only sensitive to 'horizontal' and 'vertical' directions instead of many directional Morlet wavelets (as done by Ma et al [11]), follows the same spirit as the method of Kreis [8] who used two Fourier transforms, once with a horizontal pass-band and once with a vertical one. And indeed, the innovations introduced in the following steps could also be introduced in images treated with the method of Kreis [8]. However, as already mentioned previously, the use of wavelets is still interesting as it can yield local information on the frequency, is more adapted to large bandwidth signals and keeps discontinuity errors local.

The next step consists in transforming these two images ('horizontal' and 'vertical') into a combined image. For the scale and amplitude image, this is straightforward and is just based on which direction has the highest amplitude. This is found by a pixel by pixel comparison of the two matrices shown in Fig 1(d) and (e). In this way, for each pixel the information coming from the scale (horizontal or vertical) which yields the largest cross-correlation is used. This results in the image shown in Fig 1(i) for the local amplitude, and leads to a direction-insensitive result (and also for the local scale which is not shown here). However, before the phase image can be combined in the same way, the sign ambiguity needs to be resolved. As mentioned in the introduction, three different procedures will be proposed for this step in section 2.D. Sticking to the simplest version here, it can be seen that the right 'half' of the drop in Fig 1(b) has a different sign than the left part. This is best seen in the centre of the drop, where the right part is white ( $\pi$ ) whereas the left part is black ( $-\pi$ ). Similarly, the top part of Fig 1(c) has a different sign than the bottom part. Thus, a simple flipping of the signs is all what is needed for these simple images. To this end, the horizontal and vertical sign-flipping masks shown in Fig 1 (f) and (g) are constructed. The sign of the phase is then flipped on the black side of the mask. After this flipping of the signs of the two phase images, a similar combination as for the magnitude can be performed to yield a sign-resolved phase image, which is shown in Figure 1(h). Exactly how these phase-flipping masks are constructed is discussed in section 2.D.

Then, one needs to separate the image of the droplet from the background in the segmentation step discussed in section 2.C. As should be clear from Fig 1(i), the wavelet amplitude calculation results in a very clear separation from the background, as the droplet yields a

quasi-uniform high intensity signal with respect to the black background. This step thus also sets the location of the contact line.

Once this is established, the phase signal can be unwrapped and transformed into the real height as shown in section 2.E. As the measurement up to this point is only relative, it needs to be made absolute by placing the unwrapped phase at the contact line equal to zero. From this final height map, a straightforward calculation of the volume and contact surface is possible.

A final and unique possibility of the current analysis technique is the fact that the local interface slope can be extracted immediately through manipulation of the obtained best-fitting scale estimation as explained in section 2.F. Thus, extracting the local angle along the above-defined contact line pixels will then automatically result in a local contact angle estimation (free from any shape-fitting of the droplet profile), even for non-axisymmetric droplets.

## 2.B. Wavelet Transform Processing

### 2.B.1. Building the Wavelet Transform Matrix

The Fan wavelet, as introduced by Antoine and Murenzi [36] and Kirby [37], is in essence a summation of several directional 2D Morlet wavelets spaced along different directions in order to have a direction-insensitive amplitude response. Its formula is given in Eq. (1):

$$\Phi_F(x, y) = \sum_{j=0}^{N_\theta-1} \exp[i k_0 (x \cos \theta_j + y \sin \theta_j)] \\ \times \exp\left(-\frac{1}{2} (x^2 + y^2)\right) \quad (1)$$

with  $\theta_j = \theta_0 + j\delta\theta$ . The best choice for  $\delta\theta$  was investigated in [37] and was found to be  $16.29^\circ$  for  $k_0 = 5.336$ . Thus, for the predominantly vertical directions, a set of 8 Morlet wavelets (i.e.  $N_\theta = 8$ ) symmetrically distributed in the top half of the Fourier space is used which is capable of measuring angles from  $\pm 20^\circ$  (i.e.  $\theta_0 = 20$ ) to  $\pm 160^\circ$ . For the horizontal directions, simply the transpose of the input image is analysed and retransposed afterwards.

The next decision to make is which scales of the mother wavelet will be analysed. As the complex Morlet wavelet, which lies at the basis of the Fan wavelet, is in essence a sine function modulated with a Gaussian window, the scale of a Fan wavelet is directly linked to the local period of the underlying sine function. Through calibration on perfect sinusoidal images we found that the period is equal to 1.2 times the scale of the wavelet in our case. Now, as the sinusoidal appearance of our signal is coming from the local slope

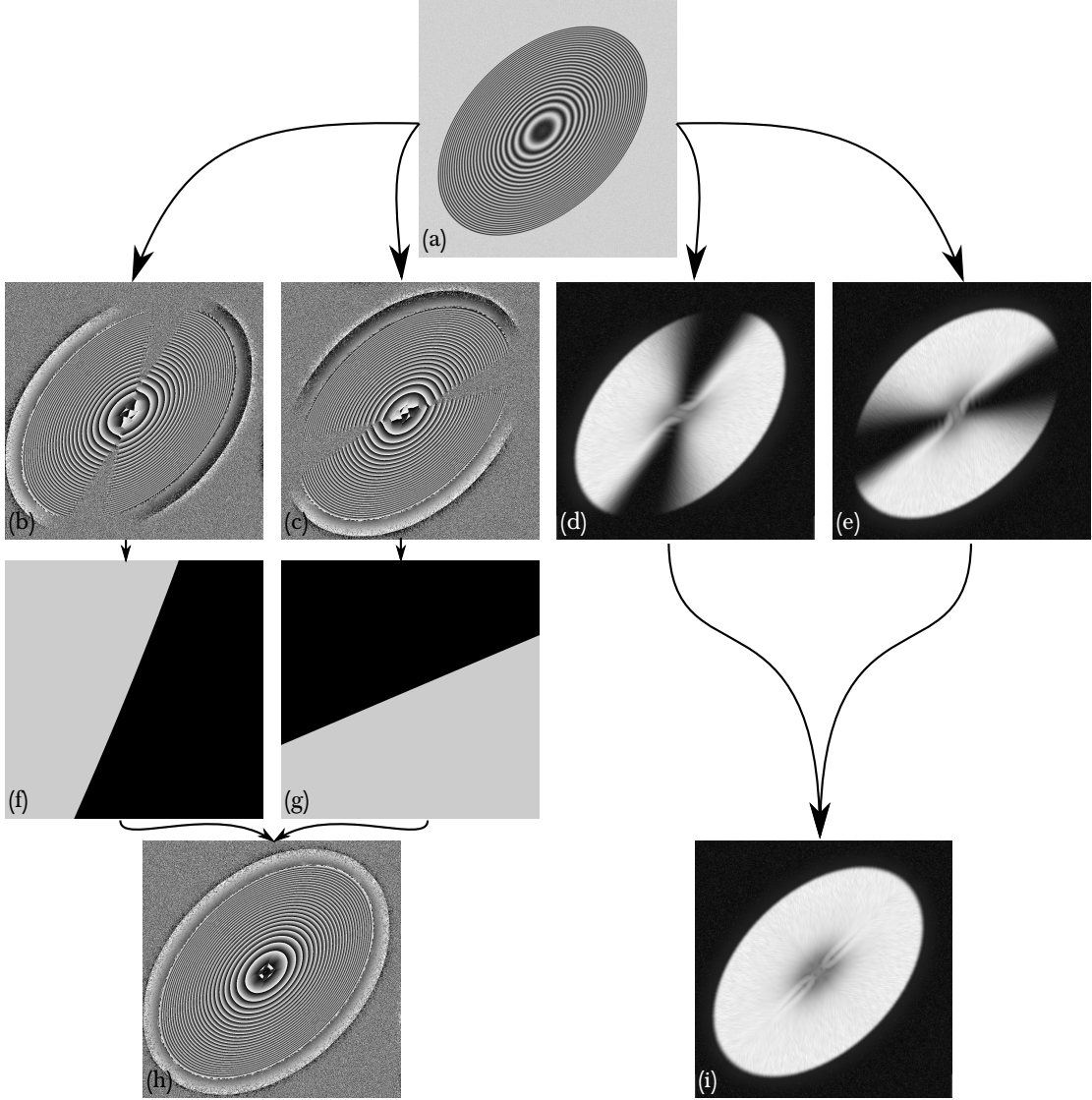


Fig. 1. Overview of the image processing chain. The input image (a) is analysed to yield two phase images (b) and (c), two amplitude images (d) and (e) and two local scale images (not shown). The local amplitude images can be combined directly to yield image (i), but the sign ambiguity in the phase images needs to be resolved first before the recombination. This is done with the two 'phase-flipping masks' (f) and (g). The resulting combined phase image is shown in (h).

of the interface, one can extract information on the gradient of the phase (without the need for an extra differentiation step) from the obtained local scale of the best-fitting wavelet. This was already used for strain measurements in [32]. This also implies that there is a direct correspondence between the scales that we choose and the slopes or angles that we want to fit our surface with. Thus, the definition of the different scales and their resolution is prescribed by the slopes we expect to have in our system and with which level of accuracy we want to measure them. Knowing that a single period in a Mach-Zehnder interferometer corresponds to a height change of  $h_f = \lambda / (n - 1)$  with  $\lambda$  the wavelength of

the laser and  $n$  the refractive index of the liquid, we find that the local interfacial angle  $\theta$  is equal to:

$$\theta = \arctan \frac{h_f}{1.2 s \text{ pix}} . \quad (2)$$

Here,  $s$  is the local scale of the mother wavelet and  $\text{pix}$  is a calibration constant to transform an amount of pixels into millimeter. Thus, discretising the  $s$ -space is equivalent to discretising the measurable local angles and ultimately the contact angles. This discretisation can be performed in many ways. One approach could be to obtain a constant resolution of e.g.  $0.2^\circ$  in the angle measurement. As our measured contact angles

are in general  $< 20^\circ$ , this corresponds in effect to an inverse linear discretisation :  $s_i = \alpha/\theta_i$  with  $\theta_i$  going from a minimum to a maximum angle with a given increment (e.g.  $0.2^\circ$ ) and  $\alpha$  a setup-dependent parameter. The downside of this choice however is the uneven procentual errors made when measuring different contact angles. Contact angles close to  $1^\circ$  can only be measured with at best a 10% uncertainty, whereas  $10^\circ$  is measured with a precision of 1%.

An alternative choice, which is pursued here, is to aspire a constant procentual error  $\epsilon$  for any given local angle. Thus, approximating the error by forward differencing and seeing as the procentual error on the angle is approximately the same as that on the inverse of the scale (for small angles), we search the discretisation of the scales  $s_i$  for which the following holds:

$$\frac{\frac{1}{s_i} - \frac{1}{s_{i+1}}}{\frac{1}{s_i}} = 1 - \frac{s_i}{s_{i+1}} = 2\epsilon.$$

For which the following constructive formula can be deduced starting from a given starting scale  $s_{min}$  (typically equal to the Nyquist limit of 2):

$$\begin{aligned} s_0 &= s_{min} \\ s_i &= \frac{s_0}{(1 - 2\epsilon)^i} \end{aligned} \quad (3)$$

or alternatively:

$$\ln(s_i) = \ln(s_{min}) - i \ln(1 - 2\epsilon) \quad (4)$$

Thus, we find that a logarithmic discretisation of scale-space is recovered. While this is a standard option in for instance Matlab, the current derivation will allow for an informed decision on the spacing constant depending on the desired precision in the frequency measurement. Now in practice, the smallest and largest scales ( $s_{min}$  and  $s_{max}$ ) necessary are prescribed by the image. With Eq. (3) or (4), one can then discretise the scale-space given a maximum allowable error  $\epsilon$ . Typically, around 90 different scales are used experimentally going from  $s_{min} = 2$  to  $s_{max} = 78$  which yields a precision in the local angle measurement of  $\pm 2\%$ .

As a side note, remark that this discretisation procedure turns out to have the same qualitative shape as the one given in [34] when setting  $\epsilon$  equal to  $0.5 - 0.5/q$  where  $q$  was defined in their paper to be a parameter depending on the standard deviation of the gaussian envelope used in the Morlet wavelet (equal to 1.3055 here). Reinterpreting their results from the current analysis, it turns out that a precision of about  $\pm 12\%$  in the

frequency measurement is obtained with their proposed discretisation. Remember however that their objectives were different as they wanted to determine the minimum amount of scales one needs in order to still obtain a correct phase measurement. As such, the value of 0.12 can be seen as the maximum value of  $\epsilon$ , for which the phase measurements are still reliable, but which nevertheless yields a low precision local angle measurement precision. Thus, if only the phase is required, only 15 scales instead of 90 can be used in the present application, which reduces the processing time considerably.

Continuing on this minimal discretisation procedure described in [34], it is important to note that the amplitude image (such as shown in Fig 1(i)) will in this case be very non-uniform inside the droplet, reaching a maximum when the local frequency corresponds to a used scale and a minimum when in between fitting scales. It is clear that such an amplitude image is a more difficult target for the background-foreground segmentation. A small empirical study on the procentual amplitude oscillations  $\Delta M/M$  over the image versus  $\epsilon$  was performed and we found that  $\Delta M/M \approx 18\epsilon^2$ . No detailed study was performed on the maximum amplitude oscillations allowed to maintain a reliable edge detection as a function of the noise level, but a value of  $\epsilon = 0.05$  (corresponding to  $\Delta M/M = 0.04$ ) did seem to give sufficiently smooth amplitude images. This can reduce the amount of scales from 90 to 37, thus speeding up the algorithm when no local frequency information is needed.

## 2.B.2. Performing the 2D Wavelet Transform Processing

In essence, the continuous wavelet transform performs the cross correlation of the signal with each of the different scales of the mother wavelet. Thus, cross-correlating the 2D input signal with a range of 2D scaled wavelet signals will result in a 3D output. As is well known, a cross-correlation for larger kernels can be computed faster by multiplying the Fourier transforms of the two components and performing an inverse Fourier transform on the result. Therefore, a fast implementation procedure consists in precomputing the Fourier transform of all the scales that will be used and storing this 3D matrix in RAM when treating consecutive images or on disc between experiments. Thus, this important cost does not need to be repeated for each analysis.

The algorithm then does the following. First, compute the FFT of the image and multiply this FFT with each of the different scales present in the precomputed 3D matrix. Then, the inverse FFT is applied to the full 3D matrix using FFTW but only along 2 axes (in essence calculating a whole range of 2D inverse FFT's in a single command). The amplitude of this 3D com-

plex matrix is calculated and a search is then conducted which yields the scale that gives the maximum amplitude for each pixel. The final resulting 2D complex matrix is composed of the complex values for the scales that yield the maximum amplitude in each pixel. Also the mentioned scale is recorded for each pixel and will ultimately give us the local slope of the interface.

All of this is summarised in the following (non-optimised) Python code where as input there is  $I$ , the input image and  $WAV$ , the 3D matrix containing the precalculated Fourier transform of the different wavelet scales. As output there is  $Freq$ , which is the index of the locally best-fitting scale and  $CF$ , a complex matrix. The magnitude of  $CF$  yields the local contrast and its phase the searched after phase. Note that the last line is rather in pseudocode as the full code is needlessly long. But in essence, we extract those complex numbers from the 3D matrix that correspond to the wavelet ridge and insert them in the matrix  $CF$ .

```

 $JI = FFT2(I)$ 
 $FW = JI * WAV$ 
 $WIS = iFFT2(FW)$ 
 $MWIS = np.abs(WIS)$ 
 $Freq = np.argmax(MWIS, axis = 0)$ 
 $CF = WIS[Freq, rowRange, colRange]$ 

```

Applying the horizontal and vertical Fan wavelets in this way then yields two complex matrices. The amplitude of this matrix is given in Figure 1(d) and (e) and the phase in (b) and (c). While it is clear that in reality the contrast inside the droplet image is uniform, the amplitude image however, clearly shows a drop-off in amplitude for those directions for which the constructed Fan wavelet is not sensitive.

Finally a practical note on the chosen algorithm. It should be clear that handling such a large 3D matrix takes a lot of RAM-memory. For a  $100 \times 1024 \times 1024$  matrix, around 4 Gb of RAM is required for the full analysis. Thus, in practise it is rather the amount of RAM present in the computer which will determine the maximum resolution of the results considering the previous paragraph. While a different programmatic procedure could alleviate these RAM requirements, it is assumed to be the fastest algorithm (at least in Python) and is deemed feasible with current-day computers.

### 2.B.3. Combining the results

Next step is the combination of all three sets of images of amplitude, phase and scale obtained from the two 2D Fan wavelets. This combination is based on the local maximum amplitude, i.e. if the amplitude for a given

pixel is larger for the 'horizontal' than for the 'vertical' image, then the amplitude/phase/scale of the 'horizontal' image is used in the combined image. This combination directly leads to correct information for the amplitude and scale images, but the combined phase image is not yet correct due to the sign ambiguity problem. However, important to note is that the absolute value of the phase (i.e.  $\text{abs}(\text{phase})$ ) is already correct and this combined absolute phase map will actually be used to 'solve' the sign ambiguity problem later.

## 2.C. Image Segmentation and Contact Line Determination

For the segmentation of the image, it was found that the wavelet amplitude signal provided the clearest separation of the droplet from the background. Using the Otsu automatic thresholding technique found in OpenCV [38], the droplet was always found satisfactorily. While a segmentation based on the localisation of the maximum gradient in the magnitude was also investigated, it was found to be more sensitive to noise and required manual parameter setting. The simple automatic amplitude thresholding avoided all of these problems in a simple way. The result of this step is a mask indicating the presence of the liquid from which the pixels of the contact line can be extracted.

## 2.D. Resolving the Sign Ambiguity

### 2.D.1. Simple Phase Mask Determination

As mentioned previously, three different strategies will be explained in this subsection, which roughly correspond to three different levels in complexity of the underlying images they are capable of solving. Figure 1(a) obviously corresponds to the simplest signal to be analysed in our context as only a single stagnation point is present. However, not a lot of publications have looked at the resolution of such simple signals as significant speed-ups could perhaps be had in this case. To our knowledge only Ge et al [39] and Dehaeck et al [40] have developed a technique specific to these kinds of images. This was based on the transformation to polar coordinates of the image with the coordinate center taken at the stagnation point. In this way, the sign ambiguity problem is resolved as the phase uniformly decreases in the resulting image (if the object is a droplet). However, such a transformation is quite costly for large images and does require a good estimation of the location of the stagnation point. In addition, if the droplet is not perfectly axisymmetric, a straightforward extraction of the contact angle is not possible. As such, the present technique is deemed more promising.

Looking at the image in Figure 1(c), we clearly see that each of the obtained phase maps consists of two co-

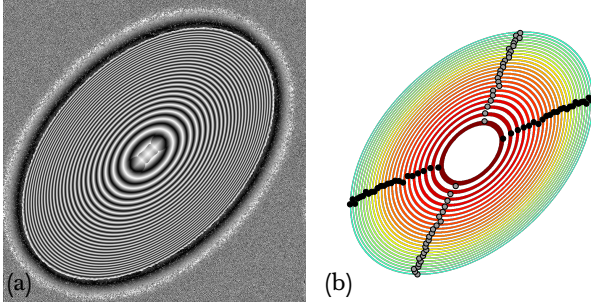


Fig. 2. Simple phase mask construction intermediate steps. (a) Absolute value of the phase. (b) Labelled closed fringes and markers used for the simple mask construction.

herent parts which need to be separated along a straight line going through the stagnation point. From Figure 1(d), it should be clear that the dip in amplitude for the 'horizontal' wavelet transform corresponds exactly to those regions where the gradient becomes vertical. And for simple phase images, these zones correspond to the maximum and minimum row attained for each of the closed fringes visible in the image. So this is the goal of the algorithm. Perform some kind of fringe skeletonization in order to extract several full fringes and draw a separating line through the locations where these fringes become horizontal.

To this end, the combined absolute phase map is used, which is shown in Figure 2(a). From this image, the location of the white (close to  $\pi$ ) and black (close to 0) fringes can be determined and analysed. For our purposes here, only one of them needs to be considered so let us take the black fringes. Casting this image to a binary image by using a threshold of  $\pi/2$  and performing a connectivity analysis, the fringes can be labelled. Here also the foreground segmentation mask found in the previous step is used. These structures are then further analysed to filter out these structures belonging to closed fringes. The end result of this processing is shown in Figure 2(b). Next to some size requirements, the main requirement here is that the center of mass of the structure should be completely encircled by the points. This is verified by checking that, after the coordinates of the constituting pixels of a structure are transformed to a polar coordinate system with the center-of-mass at the origin, a histogram analysis of the polar angle contains all angles between  $0^\circ$  and  $360^\circ$ . If this is not the case, the structure is rejected. For all of these detected closed fringes, the minimum and maximum row and column is recorded. In this way, a series of points is found which are indicated by grey points for the mask used for the horizontal images and by black points for the other mask in Figure 2(b). Thus, the 'horizontal' phase image is separated in two halves by drawing a

separating line through all of the detected gray points. This separating line is approximated as a parabola, but the exact shape is not so important as long as it goes through the 'dark' zone. An equivalent line is also constructed for the 'vertical' phase image. This leads to the two phase masks shown in Figure 1(f) and (g) where the sign is flipped in the black zones. The final correct phase image can then be constructed in the way specified in subsection 2.B.3. This very simple algorithm is capable of handling most situations reliably, which is of course helped by the fact that the black regions in the horizontal and vertical images are quite large. As such, a pixel-perfect sign-flipping mask is not necessary and in general only minor errors occurring close to the stagnation point are present. As these impact neither the volume nor the contact angle measurements, in general most of our droplet evaporation studies can be performed with this algorithm which only requires about 100ms.

### 2.D.2. Fringe Direction Determination

However, there are cases when the droplet shape becomes more exotic and a more complex algorithm is required. As already mentioned in the introduction, the sign ambiguity problem is solved in many publications by the determination of the direction of the fringes, i.e. by deciding in which direction the phase is increasing. The first step here is the determination of the orientation of the fringes which lies in the range 0 to  $\pi$ .

As mentioned, this will be done by the accumulated differences method of [19] (with a window size of 3x3). This implies calculating the following four matrices. Here,  $PP$  denotes the absolute value of the phase and the matrix notation follows that of numpy. For instance,  $PP[1 : -1, 2 :]$  implies all rows except the first and last one, and all columns starting from the third one (with index 2).

$$d0 = \sqrt{2} |PP[1 : -1, 2 :] - PP[1 : -1, : -2]|$$

$$d45 = |PP[:, -2, 2 :] - PP[2 :, : -2]|$$

$$d90 = \sqrt{2} |PP[2 :, 1 : -1] - PP[:, -2, 1 : -1]|$$

$$d135 = |PP[2 :, 2 :] - PP[:, -2, : -2]|$$

After the application of a Gaussian blurring with kernel size 3 by 3, the orientation can then be calculated from the following formula (where  $D0$  stands for the blurred version of  $d0$ ) and the arctan2 function references the standard Python/C function:

$$\theta = 0.5 * \text{arctan2}(D45 - D135, D0 - D90) \quad (5)$$

In Figure 3(a), the application to the absolute phase map of Figure 2(a) is shown with black corresponding

to 0 and white to  $\pi$ . This shows an ultra smooth result and this for a very short execution time (<0.5s). Note that other approaches such as the Gradient Method with averaging [41] gives equivalently smooth results. While this technique worked perfectly for all images, a problem did show up which was not mentioned in the original articles. When the local fringe period near the contact line approached the Nyquist limit, the algorithm failed. This is of course due to the use of a neighbourhood of 3x3 pixels for the gradient determination which is too large when the period of the signal reaches the Nyquist limit. A simple solution to this problem is by scaling the absolute phase image to twice (or thrice) its size by bilinear interpolation (with a corresponding increase in execution time).

With the local fringe orientation estimated quickly, the next problem is to transform this into a local direction. In essence, this will reinterpret a part of the local angles of Figure 3(a) to their  $\pi$  to  $2\pi$  counterparts. As mentioned, the non-continuous path following algorithm of Herraez et al [26] is used. To this end, their code is modified so as to be able to perform the required sign-unwrapping. The only modifications required were to the detection of a direction jump (which is here when the local angle difference between two pixels is close to  $\pi$ ) and in the joining rules between two pixels. In essence, there exist only two states now: either the local angle is the true direction, or  $\pi$  should be added to it (as compared to an unknown integral amount of  $2\pi$ 's in the classic unwrapping problem). Thus, in essence a binary mask needs to be constructed. Now, when joining pixel B to the group of pixel A the local angle of B is incremented with  $\pi$  if either A was already incremented and there is no discontinuity between A and B or A does not need an increment but there is a discontinuity between A and B. In programmatic terms, this can be expressed as:  $B \rightarrow incr = (A \rightarrow incr + AB \rightarrow incr)\%2$ , which states that the direction of pixel B is incremented with  $\pi$  depending on the increment bit of pixel A and on whether a direction jump was detected when comparing the direction of A and B ( $AB \rightarrow incr$ ).

Concerning the quality map that we used for the algorithm, we have constructed a two-tier quality map. The first level of prioritisation is determined by the local amplitude (and not local frequency which has only been used in literature so far for sign-unwrapping). From Figure 1(i), it is clear that the stagnation region also has a worse correlation with the wavelet. Thus, stagnation points will be analysed at the end. But, as other noise sources tend to favour high frequencies (scratches etc..) the modulation is a better indicator of overall precedence than just local frequency. This quantity is discretised in a given amount of levels (+50). For the second level,

the original quality map from [26] was used which simply avoids unwrapping the direction discontinuities till the last moment. Obviously more levels could be included in the map, but this proved to be sufficient in most cases. The final quality map is shown in Figure 3(b), where the lighter coloured zones are unwrapped last (and the black zones not at all). Note that a frequency or local scale based map would work just as well in the presented ideal case.

The resulting direction map is shown in Figure 3(c), which yields a direction going from  $-\pi$  to  $\pi$ . From this, the phase masks can be extracted easily in the following way. Where  $-\pi/2 < \theta < \pi/2$  the sign in the 'horizontal' phase image is flipped and where  $-\pi < \theta < 0$  the sign in the 'vertical' phase image is flipped. This yields the phase-flipping masks shown in Figure 3(d) and (e) where the black zones indicate where the sign of the phase is flipped. These masks are to be compared with Figure 1(f) and (g) which were obtained from the simple mask construction described in the previous subsection. Note however that there is no guarantee on the correctness of the final sign but a simple check to verify that no negative droplet volumes are obtained is enough to correct this. Finally, while this procedure is much more complex than the previous one, it is in fact still quite fast. On average only 1.2s are required for the full sign determination process (including 'sign-unwrapping') of a 1024 x 1024 image. In our opinion, this is at least an order of magnitude faster than using a directional frequency analysis technique.

### 2.D.3. Hybrid Phase-Shifting Technique

Finally, a last alternative is proposed which can solve arbitrarily complex signals at a negligible computational cost. The extra work that is required is rather in the setup as a phase shift between images needs to be imposed. This technique will use the method proposed by Kreis [8, 31] without modifications and apply it to phase images obtained from the two Fan wavelets. This method is based on the fact that the phase difference  $\Delta\varphi$  between two images will be equal to  $+\Delta\varphi$  in the region where the sign is correct and  $-\Delta\varphi$  in the region where the sign needs to be flipped. Thus, the sign-flipping mask is based only on the sign of the measured phase difference between the two consecutive images. The advantage here is obviously that its actual value is of no importance. Thus, small residual phase differences between the two images can be tolerated which implies that the current technique can be used for dynamic situations such as the ones encountered here. To highlight this, the second theoretical droplet which is generated (not shown here) has not only a known phase shift of  $\pi/2$  with respect to Figure 1(a) but is also slightly flatter. Due to this height difference, it happens that there

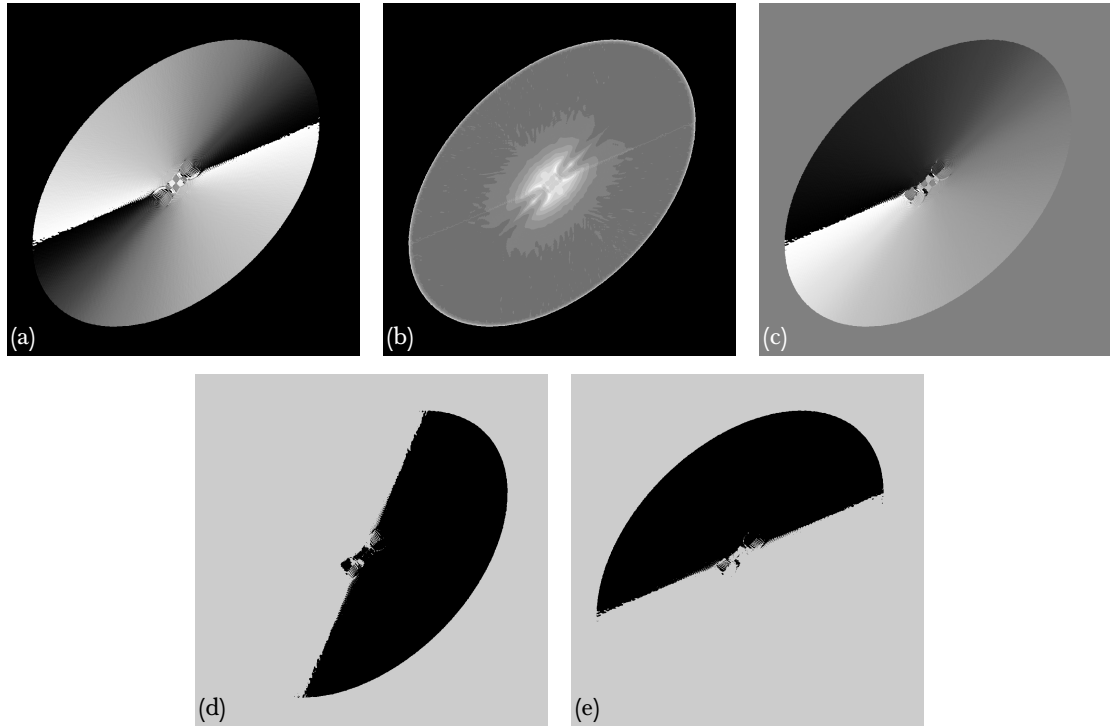


Fig. 3. Fringe direction determination procedure intermediate steps: (a) Fringe orientation map (b) Quality map to guide the sign-unwrapping (c) Direction map (d) 'Horizontal' phase mask and (e) 'Vertical' phase mask.

is a net phase difference of about  $\pi/3$  between the two images in the centre of the drop whereas the height difference at the edge stays zero. In general, such a residual phase evolution between the two images renders it incompatible with classic phase-shifting algorithms, but not with the method of Kreis [8].

For the construction of the phase masks, the WR-technique is applied to both input images. The phase shift is then calculated between the two 'horizontal' and the two 'vertical' phase images (based on the underlying complex matrices [8]). The phase shift between the two 'horizontal' phases leads to the image shown in Figure 4(a). Obviously only a coherent phase shift result is obtained in the correctly reconstructed parts. One can also see that while the phase is not constant, there is a clear colour difference between the left and right side, which corresponds exactly to the above-mentioned sign flip. Thus, from this image, the phase-flip mask in Figure 4(b) can easily be extracted from the sign of this image. An equivalent analysis on the 'vertical' phase shift will lead to Figure 4(c). These masks can be compared to Figure 1(f) and (g) for the simple algorithm and Figure 3(d) and (e) for the directional method.

As is clear from the result, the fact that the phase shift is not constant in all pixels but varies from  $\pi/2$  to  $\pi/6$  has no impact whatsoever on the precision of the final result. This makes it more appropriate for the analy-

sis of highly dynamic situations than some other hybrid techniques (e.g. Ma et al [12]). In order to quantify the maximum tolerable phase evolution between two images, we can state that the phase shift  $\Delta\varphi$  should be between 0 and  $\pi$  (or  $-\pi$ ). Now this phase shift is partly coming from the imposed phase shift and partly from the dynamic nature of the subject. Thus, when imposing a phase shift of  $\pi/2$ , a range of approximately  $\pm\pi/3$  is available for dynamic variations in the system as the analysis becomes less reliable close to 0 and  $\pi$ . In our application where a full fringe corresponds to a height difference of approximately  $2.4\mu\text{m}$ , this implies that height variations in the order of 400nm are still tolerable.

## 2.E. Phase Unwrapping and Height Determination

Now that the local phase is determined and the droplet is identified, a 2D unwrapping algorithm can be used to obtain a continuous phase map. We found that the algorithm by Herraez et al [26] yielded satisfactory results in all cases when the background was excluded in the unwrapping. The obtained phase map is however only relative. The unwrapping algorithm will start with a zero phase in a seemingly random location. The measurement can be made absolute by shifting the result so that the phase at the contact line becomes equal to

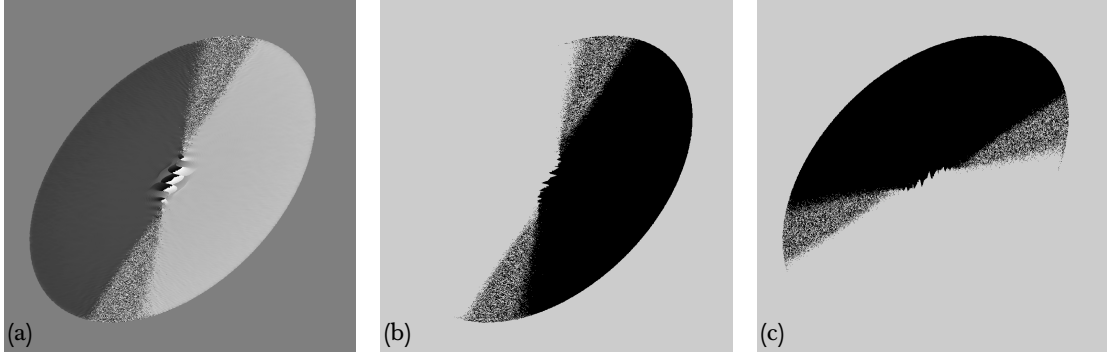


Fig. 4. (a) Phase shift measured between two phase-shifted 'horizontal' phase images. (b) 'Horizontal' phase mask. (c) 'Vertical' phase mask.

zero. The necessary shift is found by extracting the unwrapped phase value along the determined contact line position. From this list of values, the median is used as the final shift. The height information can then be retrieved by the typical relation for Mach-Zehnder interferometry:

$$H = h_f \frac{\Delta\phi}{2\pi},$$

where  $h_f$  is the height difference corresponding to a single period and  $\Delta\phi$  is the obtained unwrapped phase value.

Once the height information is retrieved, all pixels outside the mask or which yield negative heights are set to zero. This allows for an easy volume estimation as it can be obtained by simply integrating the height matrix

$$V = \text{pix}^2 \int \int H dx dy$$

where  $\text{pix}$  is the calibration value giving the amount of mm per pixel. Note that the wetted surface  $S$  can also be obtained by simply integrating the mask  $M$  (consisting of zeros and ones) as follows

$$S = \text{pix}^2 \int \int M dx dy.$$

## 2.F. Contact Angle Extraction

This part is now also quite straightforward. As we have kept the information on which scale is best-fitting for each pixel, we have an estimate for the local slope of the interface at each pixel through Eq. 2. Extracting this information along the perimeter of the drop allows us to perform a local contact angle determination or when it is assumed constant along the perimeter, obtain a precise estimate through a histogram analysis to yield the mean contact angle and its standard deviation.

A local maximal slope image is shown in Figure 5 for a different case, i.e. the axisymmetric drop shown in the inset. Note that an axisymmetric droplet was used here as the numerically generated ellipsoidal droplet used until now did not have a constant contact angle. The typical histogram for the contact angle is shown in Figure 5(b). Note that the Gaussian nature is at least partly coming from the fact that the extracted contact line pixels are somewhat scattered around the true location.

## 3. Results

### 3.A. Theoretical Benchmark

In order to obtain realistic estimates for the uncertainties of the proposed technique, theoretical interference fringes for axisymmetric droplets such as the one in Figure 5(a) were constructed with varying heights, diameters and signal-to-noise ratios. The constructed signal  $I$  is determined by the following system of equations

$$\begin{aligned} I &= a \cos(\phi + \phi_i) + n_\sigma \\ \phi &= \frac{2\pi H (n - 1)}{\lambda} \\ H &= b \left[ (x - x_c)^2 + (y - y_c)^2 \right] + c \end{aligned} \quad (6)$$

with  $a$  the amplitude of the fringes,  $\phi$  the local phase determined from the local height  $H$ ,  $\phi_i$  a random offset phase,  $n_\sigma$  a normally distributed noise with a certain standard deviation  $\sigma$ ,  $x$  and  $y$  the pixel coordinates,  $x_c$  and  $y_c$  the randomly varying droplet centre coordinates and  $b$  and  $c$  constants setting the radius and apex height of the droplet respectively. Here, the signal to noise ratio will be defined as  $SNR = \frac{2a}{\sigma}$  and the precision will generally be given by a 95% confidence interval (i.e.  $\pm 2\sigma$ ).

#### 3.A.1. Phase and height uncertainties

Figure 6(a) shows the difference in the unwrapped phase as a function of the non-dimensional radial distance to

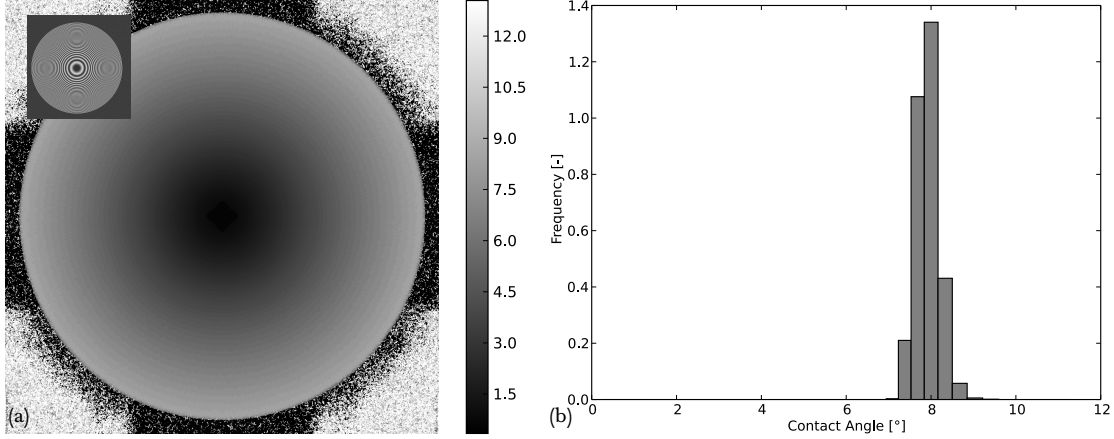


Fig. 5. (a) Local measured angle for the numerically generated axisymmetric image shown in the inset. (b) Histogram of the extracted angles along the contact line.

the droplet centre for a SNR of 14. This shows roughly that close to the central stagnation point and the contact line, the results become less precise. In the intermediate region where phase curvature [42] and signal truncation effects can be ignored [13], the phase is precise but not very accurate. This is highlighted in Figure 6(b), where the histogram is shown for the intermediate region ( $r = 0.4 \rightarrow 0.9$ ). The resulting error is Gaussian distributed with a bias of 1.36 and roughly  $\pm 0.076$  uncertainty interval (95% confidence interval). Thus, we achieve for the given noise level a precision of 1/80th of a fringe and an accuracy of 1/4th of a fringe. It is very important to separate these two effects. The origin of the bias error is clear. As mentioned, the obtained phase map after the WR analysis is only relative. This is transformed into an absolute phase by assigning a zero height to those pixels at the contact line. Now, while the proposed segmentation procedure is simple and robust, it does however not lead to a sub-pixel correct contact line determination. As such, a slight offset error in the order of 1/4th of a fringe is understandable. The precision of the measurement is coming from the WR-processing and equals 1/80th of a fringe here, which is much better than expected for a SNR of 14. However, this precision is clearly smaller near the contact line. This is unfortunate as the phase at the contact line is used to shift the entire profile to its absolute height and therefore the magnitude of the bias error is not only due to the imprecision of the segmentation procedure.

These results show the importance of a systematic analysis where the evolution of the accuracy and the precision of the phase measurement is investigated versus the SNR of the images. In Figure 7(a), the precision is shown versus the SNR for three different contact angles (for  $r = 0.4 \rightarrow 0.9$ ). This precision is expressed as the fraction of a full fringe (e.g. a preci-

sion of 1/50th of a fringe). This shows quite naturally that the precision deteriorates when the noise level increases. However, important to stress here is that the observed dependency is very small. In the inset, a zoom of an image with a SNR of 3.6 and a minimal period  $P_{min} = 7.68$  at the contact line is shown. This image can still be analysed with a precision better than 1/40th of a fringe (or  $\pm 60$  nm in the present case). In the figure, also the predicted precision of a LUT-based approach (such as used in RICM [6]) is shown by the thick solid line. For this case, the precision on the measured phase is directly proportional to the precision on the image intensity. Using  $2\sigma$  here (instead of  $\sigma$  for the determination of the SNR-level), we obtain that  $2\pi/2\sigma = SNR/2$  and this corresponds to the solid thick line in the figure. This clearly shows the tremendous advantage of some spatial averaging. Remember however that the precision for the LUT-technique is constant throughout the image, whereas our technique is slightly biased near the edge and centre of the image. A second dependency which is shown in this figure, is the one on the contact angle or rather the minimum period  $P_{min}$  found at the contact line. Clearly, noise has a larger influence when the period approaches two pixels. This is likely due to the inherent high frequency content of the random gaussian noise which is added, which can 'infiltrate' in the local bandpass filtering of the WR-technique. Note that this is also readily visible in Figure 6(a), where the error steadily increases when approaching the edge and thus larger local slopes. Further experiments on different sizes and contact angles showed that a precision of 1/50th of a fringe ( $\pm 50$  nm) for noise levels encountered in our experiments with a SNR of 14 is a realistic estimate for the intermediate droplet region.

The bias error however is much larger and leads us to consistently underestimate the phase. One reason for

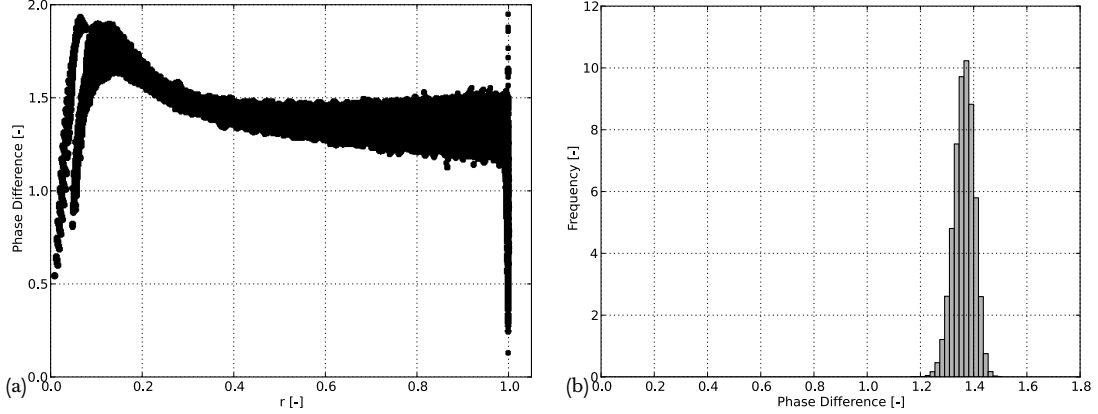


Fig. 6. (a) Phase error versus non-dimensional radial position  $r$ . (b) Histogram of error for  $r = 0.4 \rightarrow 0.9$ .

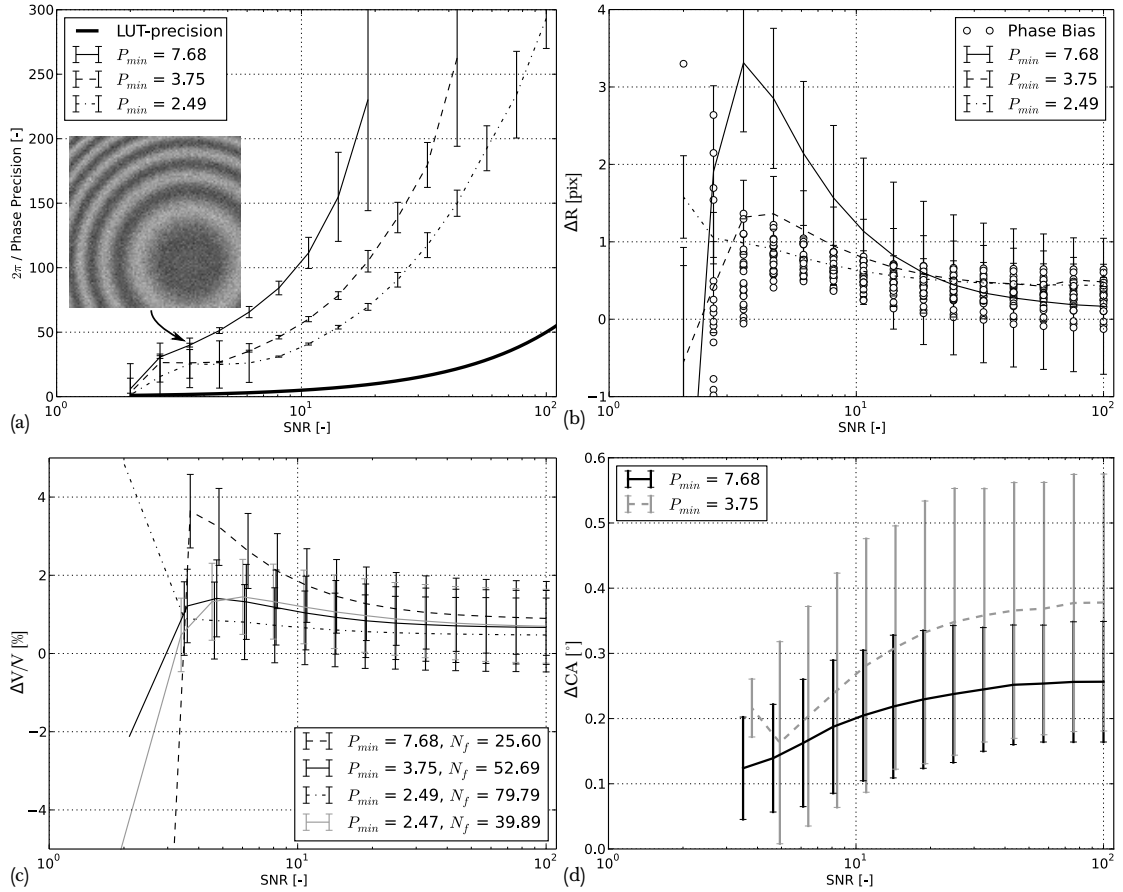


Fig. 7. (a) Precision expressed as a fraction of  $2\pi$  versus SNR. In solid, the expected precision of straightforward gray scale to phase interpretation (b) Difference in real radius and detected radius (c) Volume error versus SNR (d) Contact angle error versus SNR.

this is coming from the mask determination procedure. In Figure 7(b), the difference between the true and estimated droplet radius is shown for different contact angles. The radius estimation is derived from the droplet contact surface  $S$  through  $\sqrt{S/\pi}$ . This shows that the mask is consistently a bit smaller than the true perime-

ter. Nevertheless, a difference going from half a pixel to 2 pixels for typical noise levels, is very satisfactory for a parameter-less segmentation procedure. Now, as the local phase at a slightly shrunken perimeter is not zero, we are quite naturally making a consistent underestimation of the total phase (and height). In fact, obtaining

the phase bias from a typical histogram such as the one in Fig 6(b), and recalculating this into a masking bias leads to the circles in the figure. This shows that there is a clear correlation between the phase bias and the masking bias. However, the story is a bit more complicated in reality, as can be understood by the imperfect correspondance between the two. Near the edge, the signal truncation results in a deviation of the measured phase from the true phase as is visible in Figure 6(a). Therefore, if one would use the true droplet mask (which is known in the simulations), the phase bias will not necessarily be smaller than what is shown here. Therefore, no further optimisations were undertaken so far for the segmentation step, as one needs to solve the phase truncation errors near the perimeter first if one wants to improve the phase bias drastically. Finally, note that while the error on the mask radius is larger for larger periods at the contact line, the phase bias is nevertheless slightly better. In typical experiments, the phase accuracy was estimated to be approximately 1/3th of a fringe (800 nm). Finally, remark that the segmentation step starts to fail for  $SNR < 3.6$ .

In spite of the bias errors, the calculated procentual volume underestimation is of the order of 1 to 4% even for large noise levels, as is shown in Figure 7(c). The volume estimate not-surprisingly also breaks down when the segmentation starts failing at a SNR of 3.6. Also highlighted in this figure is the fact that this accuracy goes down for smaller contact angles. This can be understood as this corresponds to 'larger' fringes. As the central and contact-line regions where the phase is not correct roughly has the spatial extent of two fringes (due to the Gaussian envelope used in the wavelet), this means that a larger part of the drop is sized incorrectly for broader fringes resulting in larger procentual errors. Nevertheless, the volume estimate accuracy of the technique is excellent. For this graph, also the effect of the droplet size had an important influence. The fourth (gray) curve corresponds to a droplet with half the diameter as the other droplets but with roughly the same contact angle as the third curve. Yet, the bias is more similar to the second curve. Thus, the global error is rather determined by the amount of fringes  $N_f$  than the contact angle. In the figure this is confirmed as the amount of fringes of the gray curve is closer to the black solid line than to the black dash-dot line.

### 3.A.2. Frequency and local slope uncertainties

In Figure 8(a), the contact angle error is shown over the entire image for a noise-free image with black corresponding to  $-0.2^\circ$  and white to  $+0.2^\circ$ . Clear here is the discrete nature of our local angle estimate with a maximum increment of  $0.4^\circ$  between levels (for the largest

angles). Important to realise from this figure is the near-perfect direction insensitivity of our estimate. The Fan wavelet automatically picks up the scale measured perpendicularly to the fringes, which is exactly what is wanted here. In Figure 8(b), the procentual local angle error  $\Delta\Theta/\Theta$  is plotted versus non-dimensional radial distance to the centre  $r$  for two different noise levels. This shows qualitatively a similar picture as for the phase. The central and edge regions have larger errors than the intermediate range. Importantly, this intermediate range is now hardly biased. For large SNR's, the error in the intermediate region is entirely dictated by the scale discretisation procedure, which is shown by the solid lines ( $\pm 0.02\%$ ). Thus, using more scales would decrease the overall error. For a smaller SNR, noise inevitably leads to an increase of this error and this more so in the high frequency zones. As such, there is a limit to the precision that can be achieved by this discretisation procedure, which is imposed by the SNR. For the present experiments ( $SNR \approx 14$ ),  $\pm 2\%$  is a good trade-off.

While in the intermediate region there is virtually no bias, at the edge, a consistent underestimation of the contact angle does occur. This is also clearly visible in Figure 8(b) for the high SNR case. Near the edge, the black dots go down strongly, indicating the mentioned bias. In Figure 7(d), the contact angle underestimation is shown versus the SNR for two different contact angles. This shows that a little noise is not a bad thing here as it decreases the general offset. This can be understood from the following reasoning. At the contact line, the wavelet faces a discontinuous situation where a certain fringe period exists on the e.g. left hand side but on the right hand side this goes to infinity if there is no noise present. Quite naturally, the best fitting wavelet will tend to have an intermediate period, which corresponds to an underestimation of the true local angle. However, if noise is present, these noisy pixels will never line up to give an infinite period signal but will rather favour the higher frequencies. As such, the drop in frequency at the edge is less pronounced and the bias error decreases. It should also be clear that this bias quickly fades away, if the used mask is taken slightly smaller than the droplet perimeter. Nevertheless, it is clear that further study is necessary on how to reduce this bias error.

### 3.B. Practical Applications & Performance

After testing the algorithms on generated simple images, in the following they are applied to several practical examples. In Figure 9(a), a sliding droplet is shown. For applications like these, the importance of being able to calculate the contact angle all along the perimeter is very useful as it is not constant. As this image is still

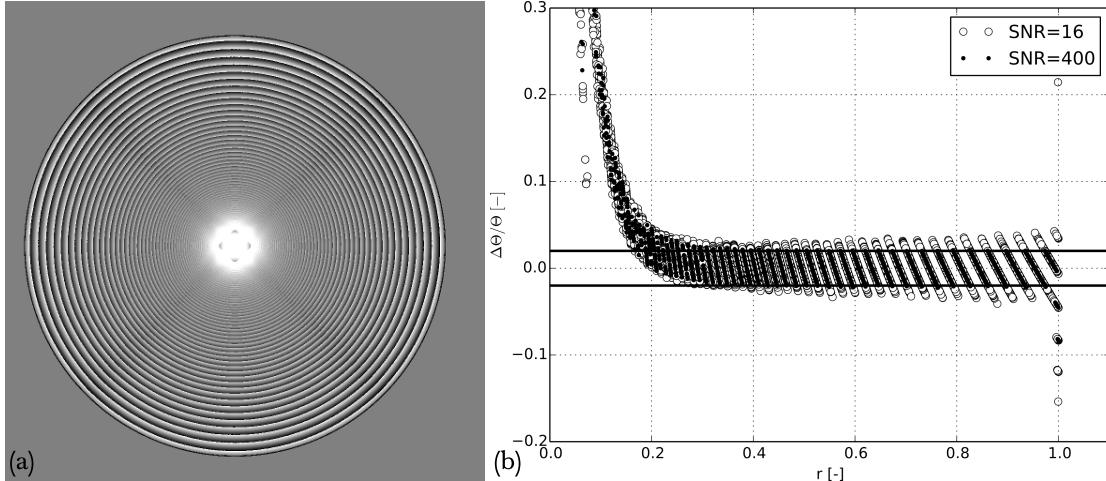


Fig. 8. (a) Local contact angle deviation from theoretical value. Black equals  $-0.2^\circ$  and white  $+0.2^\circ$ . (b) Local contact angle deviation versus non-dimensional position  $r$ .

relatively simple, the simple mask determination procedure from subsection 2.D.1 can still be used. In Figure 9(b), the separating lines for the vertical and horizontal sign flipping mask are shown. While the perfect location is not found everywhere, the tolerance to misalignment is large enough to still get a correct height map. In Figure 9(c), the local interfacial slope is shown. Remark that the measured angles at the advancing contact line are larger than in the remainder. Naturally, the two other proposed algorithms for the sign ambiguity handling are also capable of solving this image. However, the orientation-direction algorithm could have had some difficulties with the leading edge of the drop as the Nyquist limit is slightly violated there. This leads to bad orientation estimations which could induce sign-unwrapping errors. However, as aliased parts also lead to lower amplitudes, the algorithm correctly addresses these zones after the rest of the drop, leading to a containment of the problem. Note that a frequency-only based quality map experiences more problems with such zones.

In Figure 9(d), a rather unusual droplet image is shown in which multiple peaks (of unknown origin, by the way) were present near the droplet edge. The analysis of such an image is clearly too complex for the simple mask construction technique. In Figure 9(e), the obtained direction map after applying the algorithm of subsection 2.D.2 is shown. Figure 9(f) shows that with this map, the correct height map can be reconstructed. Only some difficulties exist in the large flat stagnation area, which is not a surprise.

To show an experimental validation of the proposed hybrid algorithm of subsection 2.D.3, two consecutive images are analysed of a droplet which was just de-

posited and is still spreading (only one of which is shown in Figure 9(g)). Even at 90 fps, this leads to finite thickness variations between the two images. As the contact line is moving, there is an increase in thickness for the edge pixels of the first image, while in the centre the thickness is decreasing. Now, unfortunately we do not have the equipment to make a true phase-stepping interferometer. However, due to residual vibrations in the system, a significant global phase shift was present between the two images, which was larger than the local phase variations. Using this poor-mans phase stepping setup, we are able to present at least a proof-of-principle result here. Figure 9(h), shows the measured phase difference between the two consecutive 'vertical' phase images. The sign of this image, gives us directly the phase mask that we should use for the correct combination of the phases. Figure 9(i) shows the height map for this case, where the central point with missing information corresponds to the position of the needle in the original image.

Finally, some words on the performance of the current algorithm. It was implemented in Python 2.7 using Numpy, Scipy, OpenCV and FFTW to do the matricial calculations on a four year old laptop (Intel I5-2520M with 1333Mhz RAM). Remark that we found that the clock speed of the RAM-memory was more important than the raw processor speed. With this setup, analysing 1024x1024 images using 90 scales required 8.4s. The computationally most expensive steps are the multiplication of the Fourier transform of the image with the wavelet matrix (0.5s), the inverse Fourier transform of this 3D matrix (1.2s), the ridge detection and extraction (1.9s) (which all need to be performed two times) and the phase unwrapping (0.7s). For the construction of

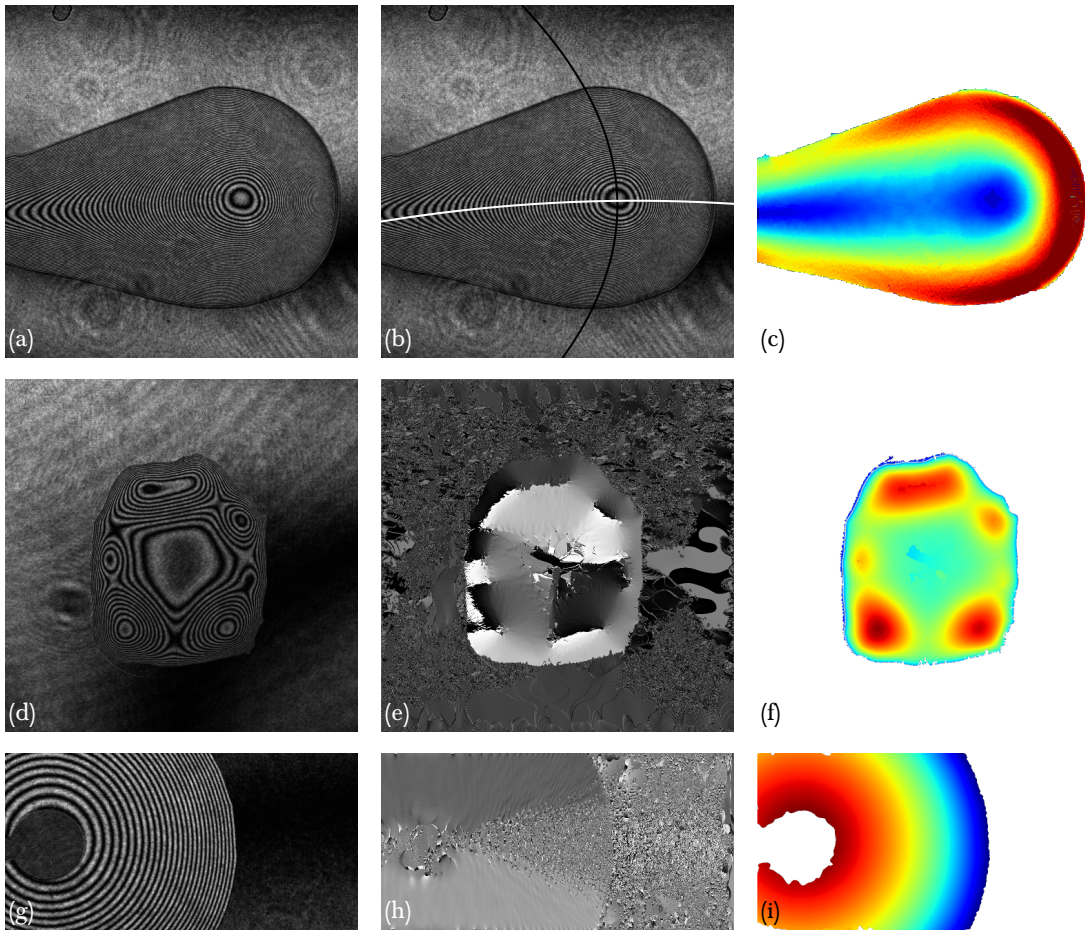


Fig. 9. Practical applications of the algorithm. (a) Sliding droplet image (b) Obtained separating parabolas used in the simple mask construction procedure from subsection 2.D.1 (c) Obtained local interfacial slope map (d) Multiple peak image (e) Obtained direction from the algorithm in subsection 2.D.2 (f) Obtained height map (g) Phase step image of wetting droplet (h) Measured phase difference between two 'vertical' images using the algorithm in subsection 2.D.3 (i) Obtained height map

the phase flipping masks, both the simple and the hybrid mask required 0.1s and the direction-based map required 0.9s. Note that the total time can be reduced to 2.6s when only 9 scales are used, but in that case no precise frequency information can be extracted.

#### 4. Conclusions and Perspectives

In the present manuscript, several improvements were suggested for the image processing chain of closed-fringe images. The use of two Fan wavelets was proposed instead of many Morlet wavelets as this offers a significant time advantage. It was also demonstrated how the scale space of these wavelets should be discretised in order to yield a constant precision in the frequency determination of the technique. For solving the sign ambiguity problem, several alternatives were proposed and tested successfully. The accuracy and precision of the resulting algorithm was then characterised by numerical experiments. This demonstrated, as anticipated, that Wavelet Ridge processing yields an excel-

lent precision even in the presence of quite some noise and only requires a single image to achieve this. Also its capability to extract local frequency information makes it superior to LUT-like image processing algorithms.

Nevertheless, some challenges remain to make it the de facto standard for analysing high bandwidth dynamic fringe images. First of all, the results near the stagnation point ( $r = 0 \rightarrow 0.3R$ ) do become relatively incorrect. While its impact for our application is not important, it is a serious flaw in the technique nevertheless. The origin of it is most probably interference with the negative frequency term and phase curvature corrections [42]. Its resolution is far from trivial, and for now a combination with a different processing technique is the most suited. One could for instance look into a pixel by pixel analysis in time if the signal is dynamic or when phase-shifting is introduced. Another option is fitting the surface with splines which are clamped to the correctly analysed region. But these options are naturally

quite time-consuming and a more automated integrated solution would be preferred. A second challenge is the analysis close to the contact line. Here, signal truncation effects might be alleviated by using one-sided wavelets (e.g. [43]). Finally, while we have been able to reduce the amount of 2D-FFT calculations needed to 180 (in our particular case) when local frequency information is needed, it is clear that further reductions of processing time are still welcome when faced with ever increasing image pixel counts. We will look into different options to face this challenge in the near future.

## Acknowledgments

The authors gratefully acknowledge financial support from EVAPORATION and HEAT TRANSFER projects funded by the European Space Agency and the Belgian Science Policy Office PRODEX Programme, and from the Interuniversity Attraction Poles Programme (IAP 7/38 MicroMAST) initiated by the Belgian Science Policy Office. PC thankfully acknowledges financial support from the Fonds de la Recherche Scientifique - FNRS. This work was also performed under the umbrella of COST Action MP1106.

## References

- [1] C.M. Vest. *Holographic Interferometry*. Wiley, 1979.
- [2] S. Dehaeck, C. Wylock, and P. Colinet. Evaporating cocktails. *Physics of Fluids*, 21(9):091108, 2009.
- [3] S. Dehaeck, A. Rednikov, and P. Colinet. Vapor-based interferometric measurement of local evaporation rate and interfacial temperature of evaporating droplets. *Langmuir*, 30(8):2002–2008, 2014.
- [4] J.D. Chen and N. Wada. Wetting dynamics of the edge of a spreading drop. *Phys. Rev. Lett.*, 62(26):3050–3053, 1989.
- [5] S.J. Gokhale, J.L. Plawsky, P.C. Wayner, and S. Das-Gupta. Inferred pressure gradient and fluid flow in a condensing sessile droplet based on the measured thickness profile. *Physics of Fluids*, 16:1942–1955, 2004.
- [6] G. Wiegand, K. Neumaier, and E. Sackmann. Microinterferometry: Three-dimensional reconstruction of surface microtopography for thin-film and wetting studies by reflection interference contrast microscopy (RICM). *Applied Optics*, 37(29):6892–6905, 1998.
- [7] J. de Ruiter, J.M. Oh, D. van den Ende, and F. Mugele. Dynamics of collapse of air films in drop impact. *Phys. Rev. Lett.*, 108:074505, 2012.
- [8] T. Kreis. Digital holographic interference-phase measurement using the fourier-transform method. *JOSA A*, 3(6):847–855, 1986.
- [9] K.G. Larkin, D.J. Bone, and M.A. Oldfield. Natural demodulation of two-dimensional fringe patterns. i. general background of the spiral phase quadrature transform. *J. Opt. Soc. Am. A*, 18(8):1862–1870, 2001.
- [10] Z. Zhang and H. Guo. Fringe phase extraction using windowed fourier transform guided by principal component analysis. *Applied Optics*, 52(27):6804–6812, 2013.
- [11] J. Ma, Z. Wang, B. Pan, T. Hoang, M. Vo, and L. Luu. Two-dimensional continuous wavelet transform for phase determination of complex interferograms. *Applied Optics*, 50(16):2425–2430, 2011.
- [12] J. Ma, Z. Wang, and T. Pan. Two-dimensional continuous wavelet transform algorithm for phase extraction of two-step arbitrarily phase-shifted interferograms. *Optics and Lasers in Engineering*, 55:205–211, 2014.
- [13] M.A. Gdeisat, D.R. Burton, and M.J. Lalor. Spatial carrier fringe pattern demodulation by use of a two-dimensional continuous wavelet transform. *Applied Optics*, 45(34):8722–8732, 2006.
- [14] M. Takeda, H. Ina, and S. Kobayashi. Fourier-transform method of fringe-pattern analysis for computer-based tomography and interferometry. *J. Opt. Soc. Am.*, 72:156–160, 1982.
- [15] J. H. Bruning, D. R. Herriott, J. E. Gallagher, D. P. Rosenfield, A. D. White, and D. J. Brangaccio. Digital wavefront measuring interferometer for testing optical surfaces and lenses. *Applied Optics*, 13:2693–2703, 1974.
- [16] M. Kass and A. Witkin. Analyzing oriented patterns. *Computer Vision, Graphics, and Image Processing*, 37(3):362–385, 1987.
- [17] Q. Yu. Spin filtering processes and automatic extraction of fringe centercenter in digital interferometric patterns. *Applied Optics*, 27(18):3782–3784, 1988.
- [18] K. Larkin. Uniform estimation of orientation using local and nonlocal 2-d energy operators. *Optics Express*, 13(20):8097–8121, 2005.
- [19] X. Yang, Q. Yu, and S. Fu. An algorithm for estimating both fringe orientation and fringe density. *Optics Communications*, 274:286–292, 2007.
- [20] H. Wang and Q. Kemao. Quality-guided orientation unwrapping for fringe direction estimation. *Applied Optics*, 51(4):413–421, 2012.
- [21] D.C. Ghiglia and M.D. Pritt. *Two-dimensional phase unwrapping: Theory, algorithms and software*. Wiley Inter Science, 1998.
- [22] M. Servin, J.L. Marroquin, and F.J. Cuevas. Demodulation of a single interferogram by use of a two-dimensional regularized phase-tracking technique. *Applied Optics*, 36:4540–4548, 1997.
- [23] M. Servin, J.L. Marroquin, and F.J. Cuevas. Fringe-follower regularized phase tracker for demodulation of closed-fringe interferograms. *J. Opt. Soc. Am. A*, 18(3):689–695, 2001.
- [24] O.S. Dalmau-Cedeno, M. Rivera, and R. Legarda-Saenz. Fast phase recovery from a single closed-fringe pattern. *J. Opt. Soc. Am. A*, 25(6):1361–1370, 2008.
- [25] H. Wang and Q. Kemao. Frequency guided methods for demodulation of a single fringe pattern. *Optics Express*, 17(17):15118–15127, 2009.

- [26] M. A. Herraez, D. R. Burton, M. J. Lalor, and M. A. Gdeisat. A fast two-dimensional phase unwrapping algorithm based on sorting by reliability following a non-continuous path,. *Applied Optics*, 41:7437–7444, 2002.
- [27] Q. Kemao and S.H. Soon. Sequential demodulation of a single fringe pattern guided by local frequencies. *Optics Letters*, 32(2):127–129, 2007.
- [28] X. Su, G. Bally, and D. Vukicevic. Phase-stepping grating profilometry: utilization of intensity modulation analysis in complex objects evaluation. *Opt. Commun.*, 98:141–150, 1993.
- [29] Sikun Li, Xiangzhao Wang, Xianyu Su, and Feng Tang. Two-dimensional wavelet transform for reliability-guided phase unwrapping in optical fringe pattern analysis. *Applied Optics*, 51(12):2026–2034, 2012.
- [30] S. Zhang, L. Xiaolin, and S.T. Yau. Multilevel quality-guided phase unwrapping algorithm for real-time three-dimensional shape reconstruction. *Applied Optics*, 46(1):50–57, 2007.
- [31] T Kreis. *Handbook of holographic Interferometry*. Wiley-VCH, 2005.
- [32] Q. Kemao, S. Soon, and A. Asundi. Instantaneous frequency and its application to strain extraction in moire interferometry. *Applied Optics*, 42(32):6504–6513, 2003.
- [33] S. Li, X. Su, and W. Chen. Wavelet ridge techniques in optical fringe pattern analysis. *J. Opt. Soc. Am. A*, 27(6):1245–1254, 2010.
- [34] J. Ma, Z. Wang, M. Vo, and L. Luu. Parameter discretization in two-dimensional continuous wavelet transform for fast fringe pattern analysis. *Applied Optics*, 50(34):6399–6408, December 2011.
- [35] M. Zhao and Q. Kemao. Multicore implementation of the windowed fourier transform algorithms for fringe pattern analysis. *Applied Optics*, 54:587–594, 2015.
- [36] J.-P. Antoine and R. Murenzi. Two-dimensional directional wavelets and the scale-angle representation. *Signal Processing*, 52:259–281, 1996.
- [37] F. Kirby. Which wavelet best reproduces the fourier power spectrum? *Comput. Geosci.*, 31:846–864, 2005.
- [38] N. Otsu. A threshold selection method from gray-level histograms. *IEEE Trans. Sys., Man., Cyber.*, 9(1):62–66, 1979.
- [39] Z. Ge, K. Kobayashi, S. Matsuda, and M. Takeda. Coordinate-transform technique for closed-fringe analysis by the fourier-transform method. *Applied Optics*, 40(10):1649–1657, 2001.
- [40] S. Dehaeck, Y. Tsoumpas, and P. Colinet. Analyzing droplets through digital holography and a 1d wavelet transform technique. In *Digital Holography and Three-Dimensional Imaging, OSA Technical Digest*, page DW3A.5., April 2013.
- [41] X. Zhou, J.P. Baird, and J.F. Arnold. Fringe-orientation estimation by use of a gaussian gradient filter and neighboring-direction averaging. *Applied Optics*, 38(5):795–804, 1999.
- [42] X. Colonna de Lega. *Processing of non-stationary interference patterns: adapted phase shifting algorithms and wavelet analysis. Application to dynamic deformation measurement by holographic and speckle interferometry*. PhD thesis, Swiss Federal Institute of Technology Lausanne, 1997.
- [43] W.J. Wang. Wavelet for detecting mechanical faults with high sensitivity. *Mechanical systems and signal processing*, 15(4):685–696, 2001.